A simple and effective 1D-element discrete-based method for computational bone remodeling

Diego Quexada-Rodríguez[$], Kalenia Márquez-Flórez[$*], M.A. Velasco[$], Olfa Trabelsi[#], Miguel Cerrolaza[§], Salah Ramtani[&], Marie Christine Ho-Ba-Tho[#], Carlos Duque-Daza [$], Diego Garzón-Alvarado[$]

[$] Universidad Nacional de Colombia (Bogotá, Colombia)
*Universidad de San Buenaventura(Bogotá, Colombia)
[#] Université de Technologie de Compiégne (Compiégne, France)
[§] Universitat Internacional de Catalunya (Barcelona, Spain) & Universitat Internacional de Valencia (Valencia, Spain)
[&] Université Sorbonne Paris Nord (Paris, France)

Abstract

In-silico models applied to bone remodeling are widely used to investigate bone mechanics, bone diseases, bone-implant interactions, and also the effect of treatments of bone pathologies. This paper proposes a new methodology to solve the bone remodeling problem using one-dimensional (1D) elements to discretize trabecular structures more efficiently for 2D and 3D domains. An Euler integration scheme is coupled with the momentum equations to obtain the evolution of material density at each step. For the simulations, the equations were solved by using the finite element method, and two benchmark tests were solved varying mesh parameters. Proximal femur and calcaneus bone were selected as study cases given the vast research available on the topology of these bones, and compared with the anatomical features of trabecular bone reported in the literature. The presented methodology has proven to be efficient in optimizing topologies of lattice structures; It can predict the trend of formation patterns of the main trabecular groups from two different cancellous bones (femur and calcaneus) using domains set up by discrete elements as a starting point. Preliminary results confirm that the proposed approach is suitable and useful in bone remodeling problems leading to a considerable computational cost reduction. Characteristics similar to those encountered in topological optimization (TO) algorithms were identified in the benchmark tests as well, showing the viability of the proposed approach in other applications such as bio-inspired design.

Keywords: bone remodeling, trabecular bone, finite element analysis, bone architecture, topological optimization.

Introduction

The bone remodeling process consists of multiple dynamic interactions between several cell types and signaling pathways that respond to different mechanical and biological conditions to repair bone damage and preserve homeostasis of needed minerals while preserving bone integrity. The main cells

involved in the process are osteoclasts, osteoblasts, and osteocytes. Insights in the understanding of bone remodeling, involving the mechanisms that couple bone formation and resorption, specifically in pathological cases such as osteoporosis which affects more than 200 million people (Sozen, Ozisik, and Calik Basaran 2017), have led to the development of mathematical models. This provides a quantitative tool to help the understanding of existing correlations between mechanical loads applied to a bone's portion and biological variables in the remodeling process, such as resorption and formation rate (Raggatt and Partridge 2010).

Five phases set up the bone remodeling process: activation, resorption, reversal, formation, and quiescence. These processes occur continually, being key aspects in understanding bone remodeling. The most relevant works found in the literature address partially or totally each one of these phases. One of the first models to relate mechanical loads to bone remodeling was Wolff's model, published in 1807. Wolff states that bone remodeling occurs in response to changes in the stress distribution in bone; this leads to a reorientation of the trabeculae. This new configuration has a topology determined by the stress field, following the principal stress trajectories (Cowin 1986). This first research established the foundations of the mechanics of modern bone remodeling, allowing for deeper research on how calcium homeostasis works, how local micro-damage repair occurs, and which biological factors are most important in this process (see for instance van Lenthe and Müller 2006 and Pivonka et al. 2008). During the mid-20th century several cell population models were developed; (Lemaire et al. 2004) relates the activation of osteoblasts and osteoclasts which depends on the RANK-RANKL-OPG signaling pathway; the model uses the mature and immature portion of the osteoblast population to control the degree of osteoclast activity. (Geris, Sloten, and Oosterwyck 2010) proposed a model using partial differential equations to describe bone formation; this approach uses a time-space scheme that varies according to cell densities and concentrations of growth factors. (Sun et al. 2013) postulated a growth-factor diffusion model in which ordinary differential equations describe signaling pathways activity. Also, this model includes agents that simulate the action of various cell types involved in vascularized bone regeneration within a CaP scaffold loaded with growth factors. (Vanegas-Acosta et al. 2011) also used diffusion models to reproduce the patterns found in different healing processes occurring in the osseointegration of a dental implant; this model helps to predict the degree of acceptance and anchoring of the implant.(Komarova et al. 2003) proposed a set of differential equations for populations of osteoclasts, osteoblasts. The model implements regulating factors to produce periodic solutions that adequately represent the biophysical process which correlates the phases of activation and resorption. The model stated by (Nackenhorst 1997) is based on strain energy as the main determinant of localized bone density in trabecular structures. This model proposed a set of bone remodeling differential equations integrated with the finite element method using 2D elements. The solution obtained resembles density distribution showing the formation of the main trabecular groups. It has been found that using

the finite element analysis to find field variables such as energy strain or stress and considering them as biological stimuli is useful in modeling other phenomena besides bone remodeling, as is the case of bone growth (Guevara et al. 2015) or viscoelastic behavior (Pawlikowski, Jankowski, and Skalski 2018). Boundary-based strategies for bone remodeling can also be found; one of the main advantages of this approach is the simplicity of the discretization since only the boundary is meshed. The use of boundary integral methods such as the Boundary Element Method (BEM) has been proposed by (Martínez and Cerrolaza 2006) and (González, Cerrolaza, and González 2009). Their results show that BEM, used together with damage mechanics, is a powerful tool in bone remodeling and adaptation. Modeling techniques such as B-spline were used in BEM-based approaches to investigate biomedical applications (Annicchiarico, Martinez, and Cerrolaza 2007). More recently, the effects of piezoelectricity in bone remodeling have been modeled using BEM as reported by (González, Cerrolaza, and González 2009), while the behavior of vertebral discs under dynamic loading was also reported by (Cerrolaza, Nieto, and González 2018).

Up to this point, bone architecture has been mainly addressed by modelling the bone trabeculae obtained from CT scans as 2D or 3D continuum elements or even 1D-beam elements arranged with different distributions (e.g. periodic honeycombs or a more random distribution). This implementation of 1D elements to represent bone architecture can reduce the model complexity thus leading to advantage from a computational point of view (Ruff1. Ruffoni, D. & Van Lenthe, G. H. 3.10 Finite element analysis in bone research: A computational method relating structure to mechanical function. Comprehensive Biomaterials II vol. 3 (Elsevier Ltd., 2017).oni and Van Lenthe 2017). Using this approach, a decrease in orders of magnitude of the number of nodes has been found, allowing a 1000-fold reduction in CPUs time in the modelling of trabecular bone mechanical properties (van Lenthe and Müller 2006).

In the field of cellular materials, a common technique to model its behavior is that of homogenization which focus on the microscopic level to predict how the structure will behave macroscopically, with this technique the structure is treated as a homogenized material rather than a discrete structure (Daxner 2010), one way to achieve this and that will be used in this paper is the discrete microfield approach which uses beam theory (using 1D elements) to predict the behavior of the microstructure of the material. In the field of bone mechanics, the homogenization technique has been used before to analyze failure properties of trabecular bone which is of interest in the understanding of bone-implant interface mechanics (Ganghoffer and Goda 2018).

For these reasons, we propose a 1D-element discrete method for the bone remodeling problem, being its main attractiveness the use of elements that resemble trabecular bone and its low computational cost. This procedure enables researchers to increase the sample size and the complexity of trabecular bone.

Until now, there are no models using this 1D approach to solve the bone remodeling problem. Therefore, we present a methodology based on the approach used by (Garzón-Alvarado and Linero 2012) which employs a dimensionless density that depends on the energy strain (see Eqn. 1) and uses different integration schemes like Heun, Euler and Runge-Kutta to solve this equation, where the use of one scheme or another did not lead to any appreciable difference. The change over time in density λ depends on variables k_1 and n which are found experimentally, the energy strain U in each step is divided by a reference strain energy value U_{ref} that determines the limit at which remodeling occurs. The work of (Garzón-Alvarado and Linero 2012) is of great importance for the proposed methodology since it is able to correctly model the behavior of trabecular bone using 2D continuous elements.

The implemented remodeling methodology has one additional feature in comparison with the (Garzón-Alvarado and Linero 2012). This paper proposes a new approach to model the bone remodeling problem based on previous works with a low computational cost compared with methodologies using continuum domain elements (van Lenthe and Müller 2006), allowing the implementation of more complex structures and sample sizes in the simulation of bone remodeling dynamics and bio-inspired conceptual designs.

Methods

In this section, the bone remodeling model is presented as well as the developed algorithm. In addition, two benchmark tests (Valdez et al. 2017) are analyzed for validation purposes.

Model description

The proposed remodeling algorithm is shown in Fig. 1, where the constitutive elements of the domain correspond to either frame or truss finite elements. To create this model the coupling of the moment equation (Eq. 2) with the density equation (Eq. 1) is required in order to relate the strain energy to the element density, thus setting the bone remodeling dynamic. This modifies the modulus of elasticity as observed in equation (Eq. 3), where $E(\lambda)$ is the elastic modulus, λ is the dimensionless density, and n is an exponent found experimentally. In equation (Eq. 2) σ is the stress tensor and b the body forces vector.

$$\frac{d\lambda}{dt} = k_1 \left[\lambda^{n-1} \frac{U}{U_{ref}} - 1 \right] \qquad \text{Eq. 1}$$

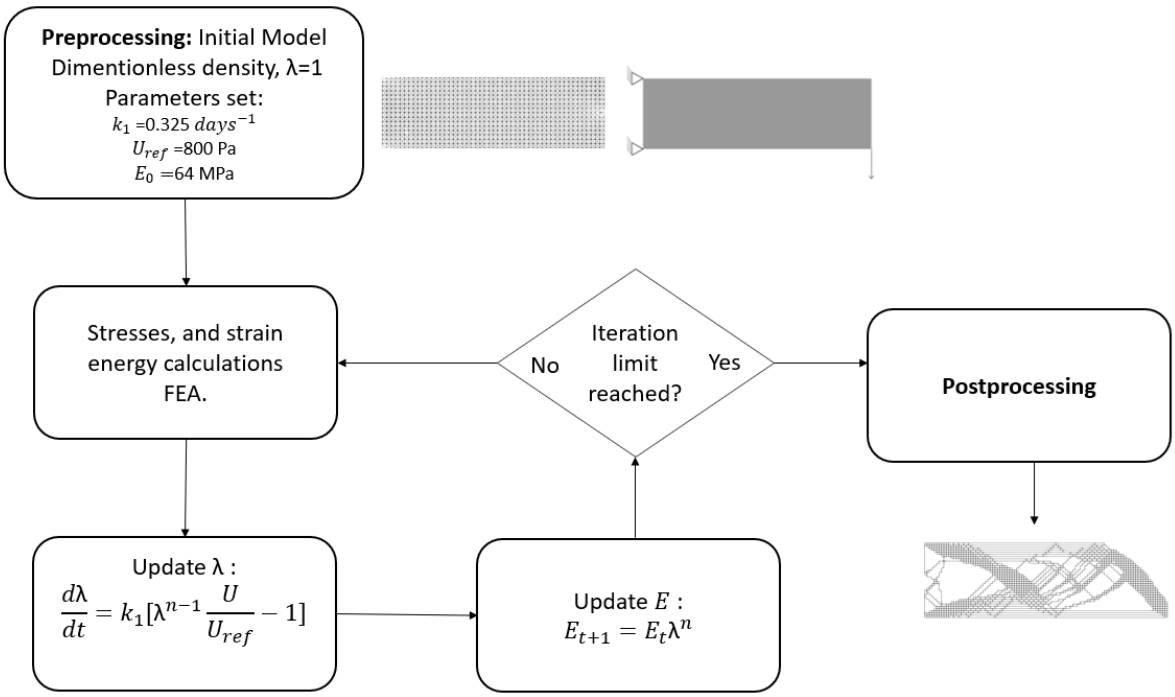

Fig. 1: Proposed algorithm

$$\nabla^T\sigma + b = 0 \qquad \text{Eq. 2}$$

$$E(\lambda) = E_0\lambda^n \qquad \text{Eq. 3}$$

To find the maximum stress, superposition was used in a fiber of an element by adding both the stresses due to the axial load P and the stresses due to the maximum bending moment M_{max} (Eq. 4). It should be remarked that the loads and moments are applied at the corresponding nodes. Each element is assumed to have a circular cross-section area *A*, moment of inertia *I* and a vertical distance away from the neutral axis *C* . M_i^{left} and M_i^{right} are the concentrated moments at both ends of the element (Eq. 5).

$$\sigma = \frac{P}{A} + \frac{M_{max}C}{I} \qquad \text{Eq. 4}$$

Similarly, deformation energy due to axial load and bending moments is expressed as:

$$U_{strain} = \frac{1}{2}\int_0^L \frac{{P_i}^2}{EA}dx + \frac{1}{2}\int_0^L \frac{M^2(x)}{EI}dx \qquad \text{Eq. 5}$$

Solving these integrals yields the strain energy, as stated by (Makris, Provatidis, and Rellakis 2006),their mathematical derivation can be found in the annexes:

$$U_{strain} = \frac{1}{2}\sum_{i=1}^{N}\left[\frac{{P_i}^2 L_i}{E_i A} + \frac{1}{3}\cdot\frac{(M_i^{left})^2 + (M_i^{right})^2 + M_i^{left}\cdot M_i^{right}}{E_i I}\cdot L_i\right] \qquad \text{Eq. 6}$$

For the 3D implementation the frame element formulation has twelve degrees of freedom since each node can have three translational displacements (Along the x,y and z axes) and three rotational displacements around each axe. The methodology flow chart shown in Fig. 1 was applied to the 3D case as well, the direct formulation and same remodelling equation is used, yet, in this case the strain energy per element takes into account terms due to torsional and additional bending moments because of the three dimensional nature of the problem, for this reason inertia along the Y and Z axis is considered, as well as the polar moment of inertia *J* and torsional modulus *G* as shown in the next equation, T is the torsional moment at the element nodes.

$$U_{strain} = \frac{1}{2}\int_0^L \frac{{P_i}^2}{EA}dx + \frac{1}{2}\int_0^L \frac{{M_z}^2(x)}{EI_y}dx + \frac{1}{2}\int_0^L \frac{{M_y}^2(x)}{EI_z}dx + \frac{1}{2}\int_0^L \frac{T(x)}{GJ}dx \qquad \text{Eq. 7}$$

Numerical implementation

To solve the finite element equations for frame and truss elements, a user element subroutine (UEL) was used and attached to ABAQUS (2017), where a direct formulation was programmed to each discrete element, Fig. 2 in the annexes has a graphical description on the methodology for this task. Euler's method was used to solve equation (Eq. 1) as shown in equation (Eq. 8)

$$\lambda_{t+1} = k_1 \left[\lambda_t^{n-1}\frac{U}{U_{ref}} - 1\right]\Delta t \qquad \text{Eq. 8}$$

A time step Δt = 0.1 days was used. Constant k_1 was 0.325 days $^{-1}$ and n was 2.0. The reference energy constant U_{ref}, which determines the threshold at which remodeling occurs was set to 800 Pa, these constants are based on the previous works of (Garzón-Alvarado and Linero 2012). It is worth mentioning that the algorithm stop condition was set to 100 days of simulation time, since at this time cell population dynamics have reached a quasi-steady-state (Buenzli, Pivonka, and Smith 2011) and after this time no significant change in density was appreciated during the simulations.

Unit cell topology

Unit cells of different shapes (hexagons, squares, and triangles as shown in Fig. 3) were tested in two benchmark tests: the cantilever beam displayed in Fig. 4(a), and the square plate subjected to a distributed load shown in Fig. 4(b). According to (Luxner et al. 2009)it is expected that unstructured meshes resemble better the mechanical behavior of trabecular bone since a more disordered cellular structure prevents early crack formation, once a load has been applied. Finally, it was tested which formulation (truss or frame) was most suitable for the remodeling algorithm based on the resulting

topology, and then its results compared with previous works on topology optimization and with the benchmark tests described in the next section.

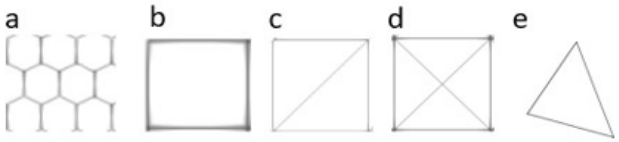

Fig. 3 Different unit cells
Different unit cells tested: (a) Hexagonal or honeycomb. (b) Square cells. (c) Triangular cells. (d) Square Cells with two diagonals. (e) Triangle.

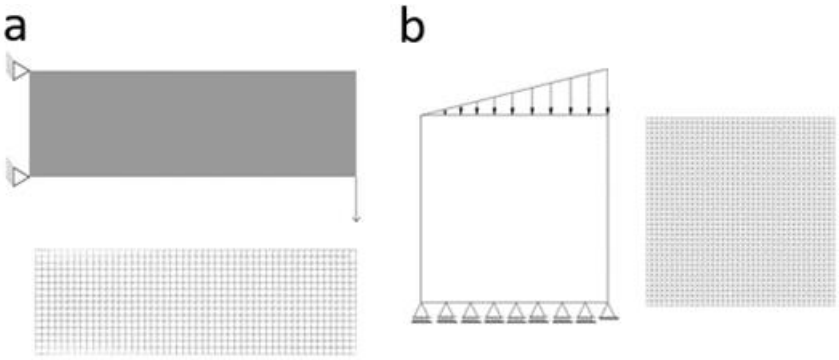

Fig. 4: (a) Cantilever beam, (b) Square plate with distributed load

Benchmark tests and model validation

In order to test the computational model, two benchmark tests were performed. First, a cantilever beam was used as the initial domain that was discretized using frame and truss elements. The meshes reproduced were made with different aspect ratios and distributions. Several element lengths (h) ranging from 2.4m to 0.15m were used to see the effectiveness of the method in each mesh. Only elements with a density higher than one (1) unit are shown in Fig. 6 to Fig. 10 to better appreciate some of the resultant topologies, whereas in Fig. 5 the continuous field of density (lambda) is shown; as the benchmark results are not the focus of the paper, only a few cases are enough to evidence viability.

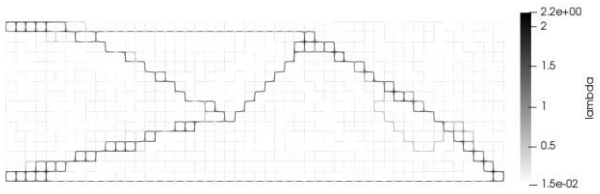

Fig. 5: Density for the cantilever beam at 100 days, element length 0.3m.

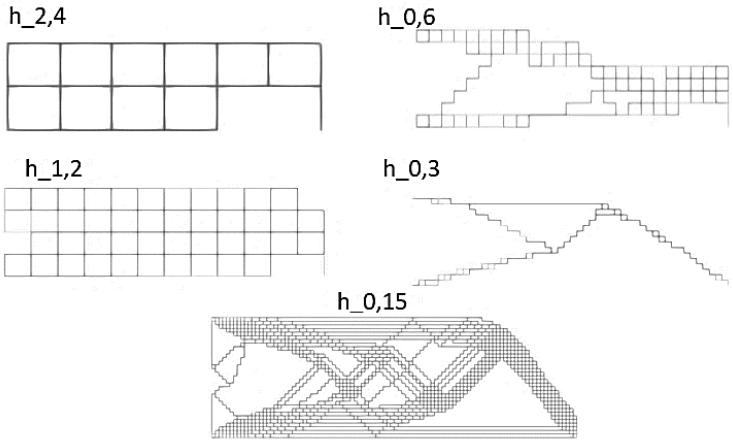

Fig. 6: Square frame cell unit structure remodeling.

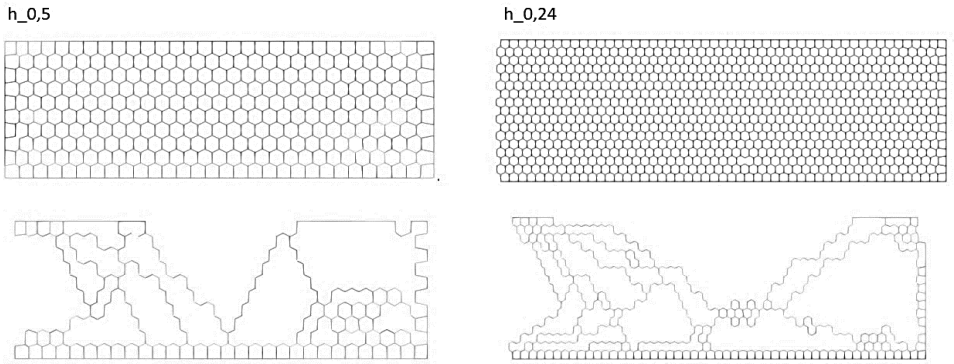

Fig. 7: Polygon cell unit structure remodeling; frame elements.

In Fig. 6 and Fig. 7 the resultant topologies of the discrete bone remodeling algorithm are shown with different element sizes and types of unit cells, while Fig. 8 depicts a triangular unstructured mesh. The results obtained with this methodology resemble those of a topological optimization (TO) algorithm for this benchmark test (Fig. 11). Examining the benchmark results, it can be noted that the method shows a high sensibility to the type of unit cell that sets up the initial domain. This can be seen in Fig. 6 and in Fig. 9 where the meshes only differ in that the square configuration has an extra diagonal element in their unit cell, yet the final topology is different since the stress distribution changes at a unit cell level.

Finer meshes produce results that seem to be more similar to those of TO algorithms, so a rather fine mesh will be used in the study cases.

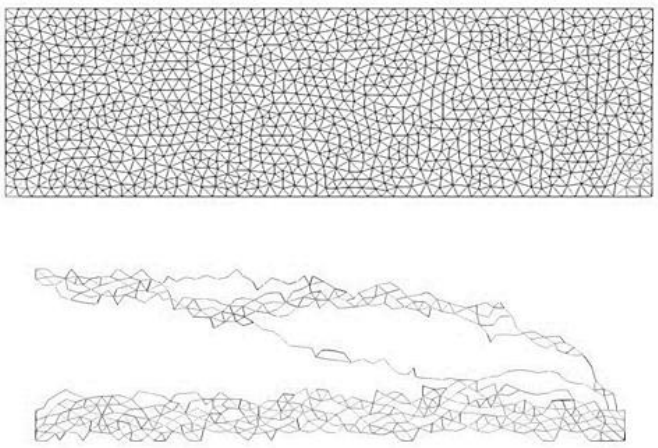

Fig. 8: Unstructured mesh remodeling with triangular unit cells.

Regarding the relationship between the topology of the unit cell and the result of the bone remodelling algorithm, there are some aspects of cellular material theory that can provide insights on what type of final topologies will be obtained and how they will behave. A classical approach was developed by Clark Maxwell, who published a paper proposing a simple equation (see Eq.9) that gives insight on the behavior of a unit cell, depending on the number of struts, b, and joints, j,(Maxwell, n.d.). In Fig. 8 a classification based on the number of joints and elements can provide information on the mechanical behavior that the final topology will have. It is good to emphasize that the algorithm will optimize shape based on strain energy per element and depending on the unit cell shape and length it will vary results, yet up to this moment we have only looked this parameters in benchmark tests to validate the model, the goal is to implement the bone remodelling algorithm in two study medical cases, where the different meshes used will resemble the topology of real bone.

$$M = b - 2j + 3 \qquad \text{Eq.9}$$

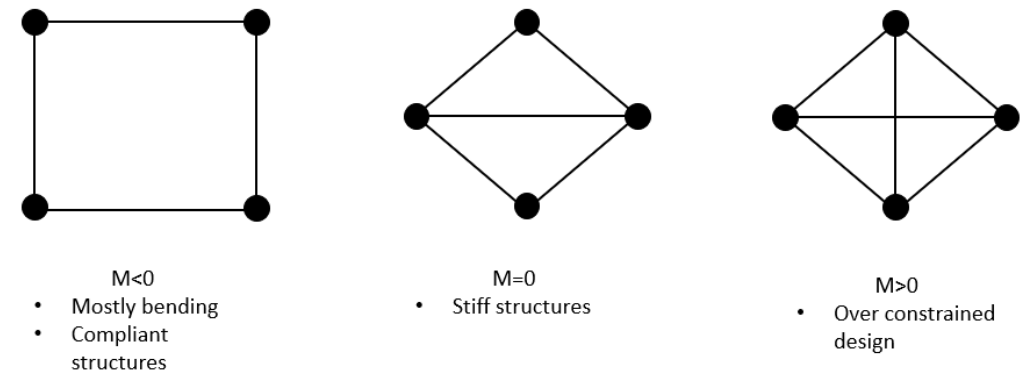

Fig 8 Maxwell, stability criterion for different structures

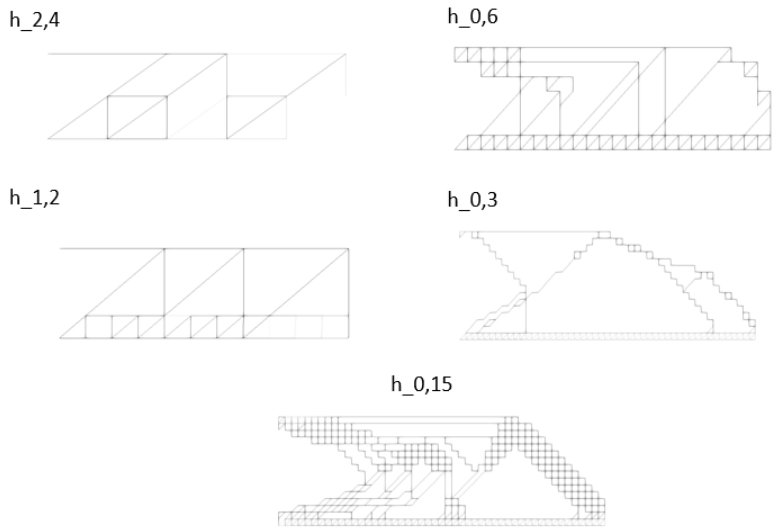

Fig. 9: Remodeling in structured meshes, triangular unit cell.

Fig. 10 displays a comparison between frame (three degrees of freedom: horizontal, vertical, and rotational displacement) and truss elements (two degrees of freedom: horizontal and vertical displacement). In this case, the capacity to bear moments is noted in the frame topology, since the final result shows a structure with longer horizontal supports, whereas in the truss case a structure with long diagonal supports at an angle of 45° is seen along the structure. Both results are structurally consistent and serve as a conceptual basis for design. It is worth noting that although there are different results in the topologies obtained, the strain energy found in the structure stays the same but concentrated along the remaining trabeculae. With the aim in mind to address bone remodelling problems, frame elements will be used in further cases, since they can bear moments, similar to trabeculae structures.

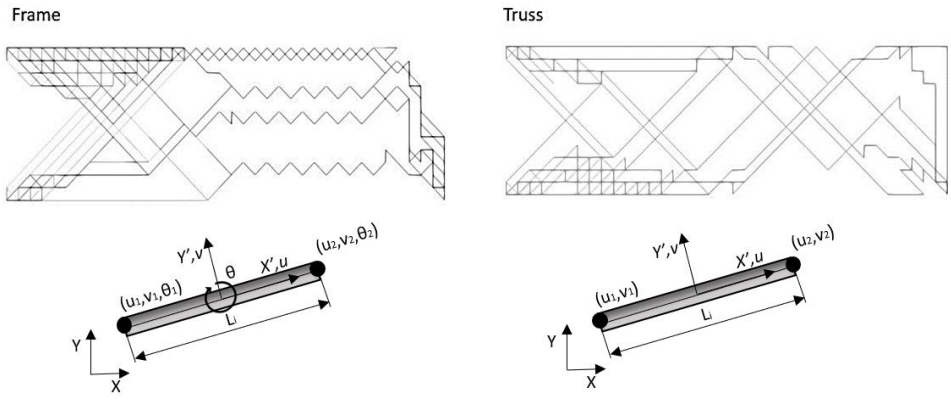

Fig. 10: Comparison between results of the bone remodeling problem using frame and truss formulation with a mesh setup by diagonal elements.

Fig. 11: Initial (left) and optimized (right) structure of a cantilever beam using a topological optimization algorithm (Chen et al., 2018)

Next, a test based on the implementation proposed by (Garzón-Alvarado and Linero 2012)is discussed herein to compare similarities in the resultant topology. A triangular distributed load is applied on a square plate with the boundary conditions shown in Fig. 12(a) a comparison was made between Garzón's results using an element-based remodeling approach (using continuous, triangular elements) and the discrete remodeling algorithm proposed herein with frame elements. In this case, an increase in speed was found with the proposed methodology for meshes with 10000 nodes. The computer used had an AMD Ryzen processor (2.30GHZ) with 7 cores and 16GB RAM. With the continuum approach a simulation time of 100 days was achieved in 310 (sec) whereas with the new methodology the simulation reached that same span in 245 (sec) wall-clock time; in this case, the proposed methodology used the unit cell shown in Fig. 3(b).

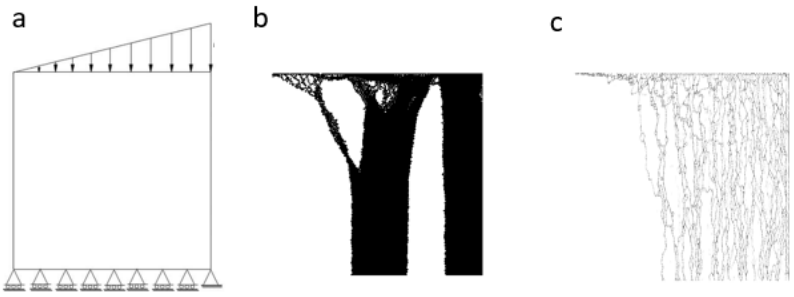

Fig. 12: Bone remodelling benchmarks
(a) Boundary conditions. (b) Result for bone remodeling problem using an element-based approach (Garzón-Alvarado and Linero 2012)(c) Result of bone remodeling problem using discrete frame elements.

To this point, two benchmark cases have been tested with the proposed methodology showing results similar to those obtained in previous works with continuum elements. In the plate model a serious of column structures are formed at the base and have ramifications at the top part. In the cantilever benchmark test a serious of diagonal structures are formed as seen in Fig. 10. This is expected in this case since the methodology follows an objective function with the purpose of obtaining a preset specific energy strain value per unit bone mass. Regarding the square plate, there are differences in the topologies obtained, but the formation of structural columns with branches are seen in both cases Fig.

12(b) and Fig. 12(c); in the discrete case, the difference in column density might be due to lack of contact between the elements that hold the highest energy density.

Given that these benchmarks showed very good agreement with previous works, two study cases will be examined to further study the reach of this methodology. For the following medical cases the geometrical properties from trabeculae were adopted from studies from (Cesar et al. 2013) on skeletal microarchitecture, for each bone.

Results

Results in 2D

In this work two medical cases were subjected to our bone remodeling algorithm in an attempt to study the formation of the main trabecular groups. The first case, proximal femur, and the second, calcaneus cancellous bone, were considered in a specific stage of the walking gait according to previous studies. The resultant topologies in both cases resemble anatomical features found in the literature reviewed.

In the first medical case, proximal femur, the boundary conditions try to mimic the loading history of this bone where the main forces correspond to both the hip reaction force and the action of the abductor muscle during the gait cycle. The loading cases are based on the works of (Beaupre and Orr 1990). The boundary conditions of the initial mesh corresponding to an unstructured lattice with a triangular unit cell are shown in Fig. 13(left). The resultant topology with the formation of the main trabecular groups (in the density field) and relevant anatomical features are seen as well in Fig. 13(right). The results show the formation of groups of trabeculae that undergo compression or tension.

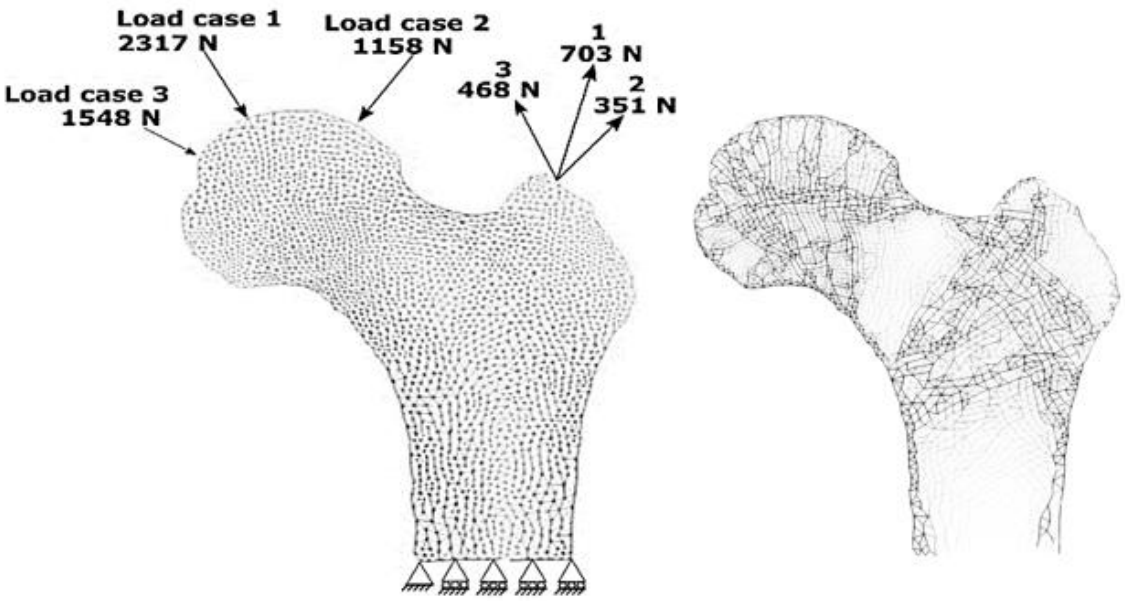

Fig. 13: Boundary conditions and topology obtained at t=100 days mass fraction, with periosteum set as a constraint.

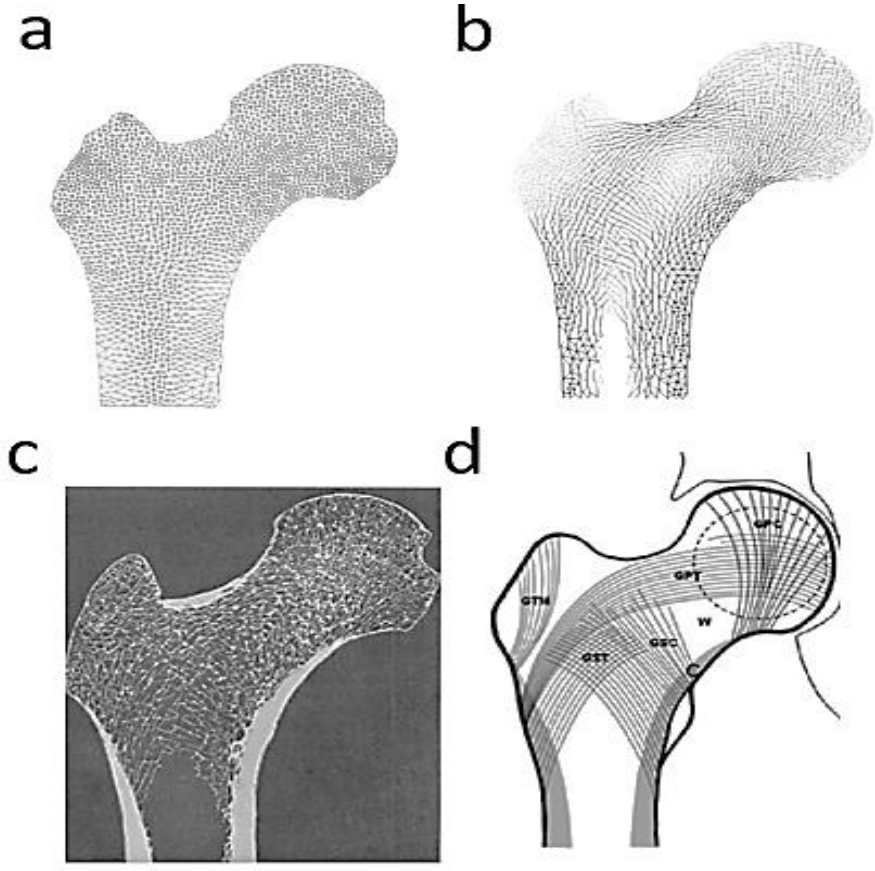

Fig. 14: Similarities in topologies obtained with bone remodelling
Bone topology (a) Study case: femur contour with initial triangular mesh and frame elements. (b) Topology obtained without restriction on the periosteum at 100 days. (c) Femoral frontal section through neutral axis, showing trabecular topology from (KOCH 1993). (d) Principal trabecular groups (Martín and Kochen 2011)

An additional condition was needed to solve these medical cases since the contour corresponding to the periosteum seemed to be affected by the remodeling algorithm. This issue was fixed by applying a constraint on each element belonging to the periosteum corresponding to a constant elastic modulus. For comparison sake, results of the femur case restrained with this condition, in Fig. 13 can be seen, whereas in Fig. 14(b) the density field is shown without the restriction.

In the second medical case, calcaneus cancellous bone, the boundary conditions were suggested by (Belinha, Natal Jorge, and Dinis 2012) which represent a series of stages of the gait cycle. The different force values at each stage are collected in Table 1, while all boundary conditions are shown in Fig. 16(a). The boundary conditions in the second stage of this cycle are detailed in Fig. 15 along with the initial mesh; results show that trabecular groups undergo, mainly, compression stresses.

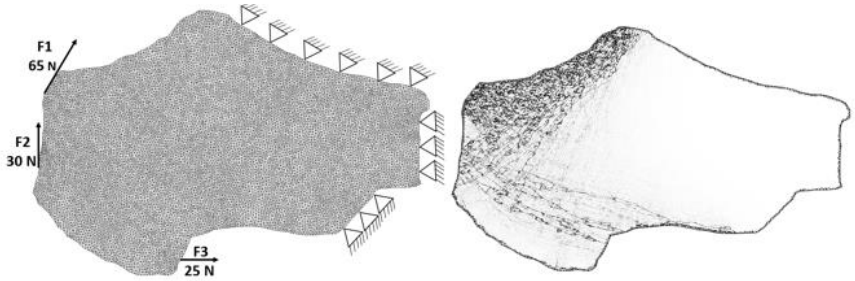

Fig. 15: Boundary conditions and topology obtained at 100 days, second load case, initial mesh is shown.

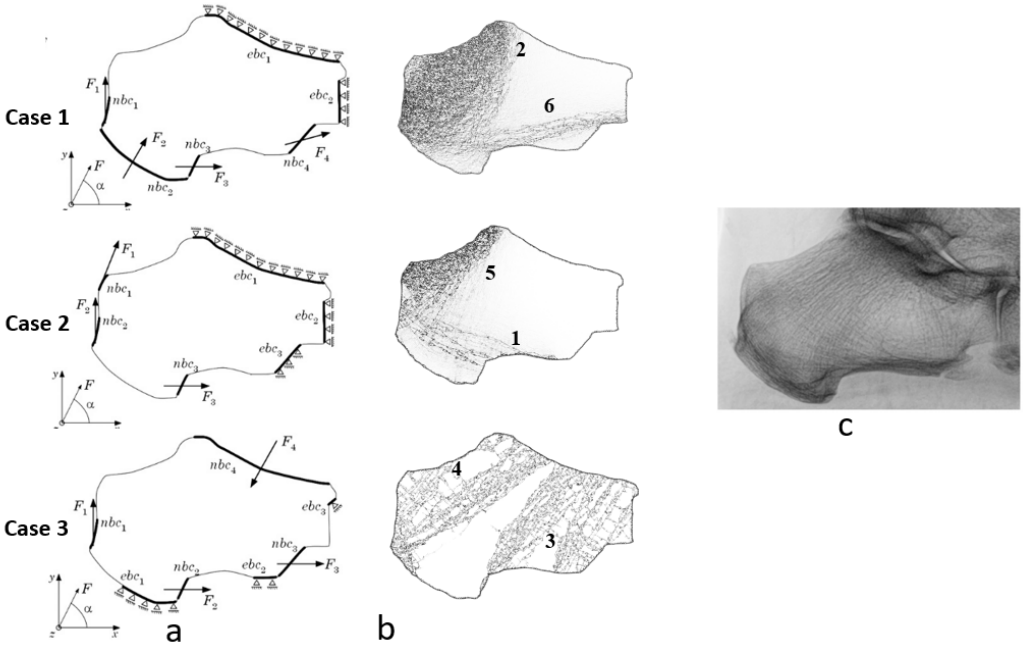

Fig. 16: Results of calcaneus cancellous bone remodeling at 100 days.
(a) boundary conditions used by (Belinha, Natal Jorge, and Dinis 2012). (b) Trabecular patterns obtained with frame elements (c) calcaneus x-ray detail.

Second medical case				
First load case	**F1**	**F2**	**F3**	**F4**
Force magnitude (N)	65	100	20	10
Direction	90°	Normal to surface	0°	5°
Second load case	**F1**	**F2**	**F3**	**F4**
Force magnitude (N)	65	30	25	--
Direction	70°	90°	0°	--
Third load case	**F1**	**F2**	**F3**	**F4**
Force magnitude (N)	65	15	15	100
Direction	90°	0°	0°	Normal to surface

Table 1. Gait cycle, boundary conditions as proposed by (Belinha, Natal Jorge, and Dinis 2012).

Implementation in 3D

As a final part of this work the authors tried this methodology in 3D as a starting point for a future work where more complex cases will be investigated. The same general methodology as in the previous 2D cases was followed, first the algorithm was tested with benchmark tests corresponding to topological optimization classical cases as the cantilever beam shown in Fig. 10 and bone remodelling cases as the one presented in Fig. 12. In the first benchmark test, the distributed load in a cube (Fig. 17), the formation of four columns is appreciated with an increased density, with arcs forming in each face, these results are similar in topology to those obtained by (Walton and Moztarzadeh 2017), allowing to infer as we did in the 2D cases that this methodology can be applied to a medical case in which the bone density equation proposed first by (Nackenhorst 1997) can yield important information on the trabecular patterns formed for a particular boundary condition.

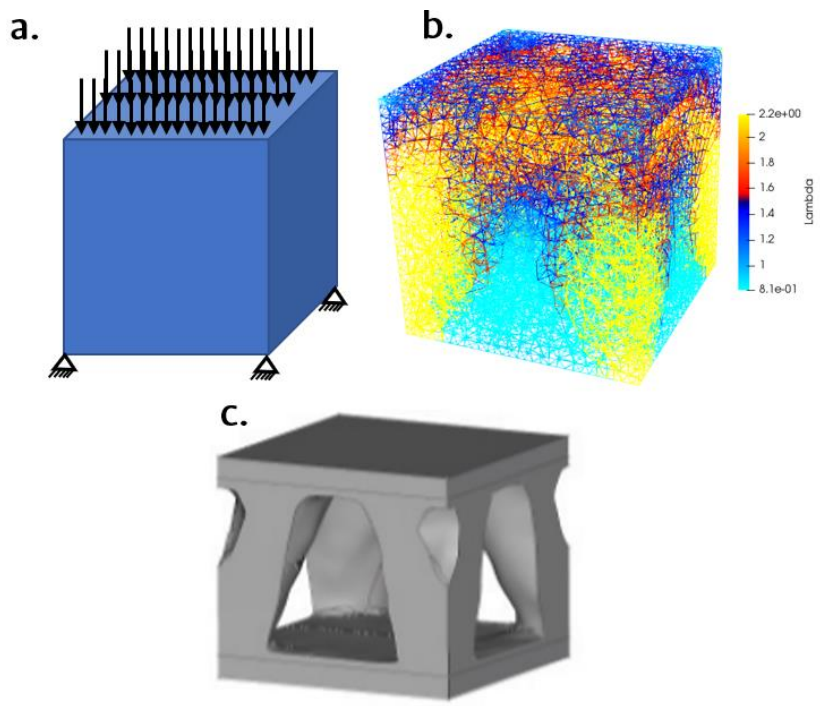

Fig. 17: a. Boundary conditions for the 3D domain. (b) Results in topology optimization for a domain composed of frame elements.(c) Topological optimization results from (Walton and Moztarzadeh 2017)

For the medical case, a 3D model of the femur was discretized into frame elements and subjected to the boundary conditions suggested by (Beaupre and Orr 1990), where an approximated pattern of the main trabecular groups was found. In Fig. 18 the 3D initial bone density is shown along with the bone remodelling results after 100 days, as in the 2D simulations for this medical case. The mesh is composed of tetrahedral structures (i.e., the unit cell is a tetrahedron). The properties of each element are the same as in the case of the previous 2D simulations, inertias, area, and average length per element (Cesar et al. 2013). For these simulations a restriction in density was set for the elements corresponding to the periosteum as in the case of Fig. 13Fig. 13.

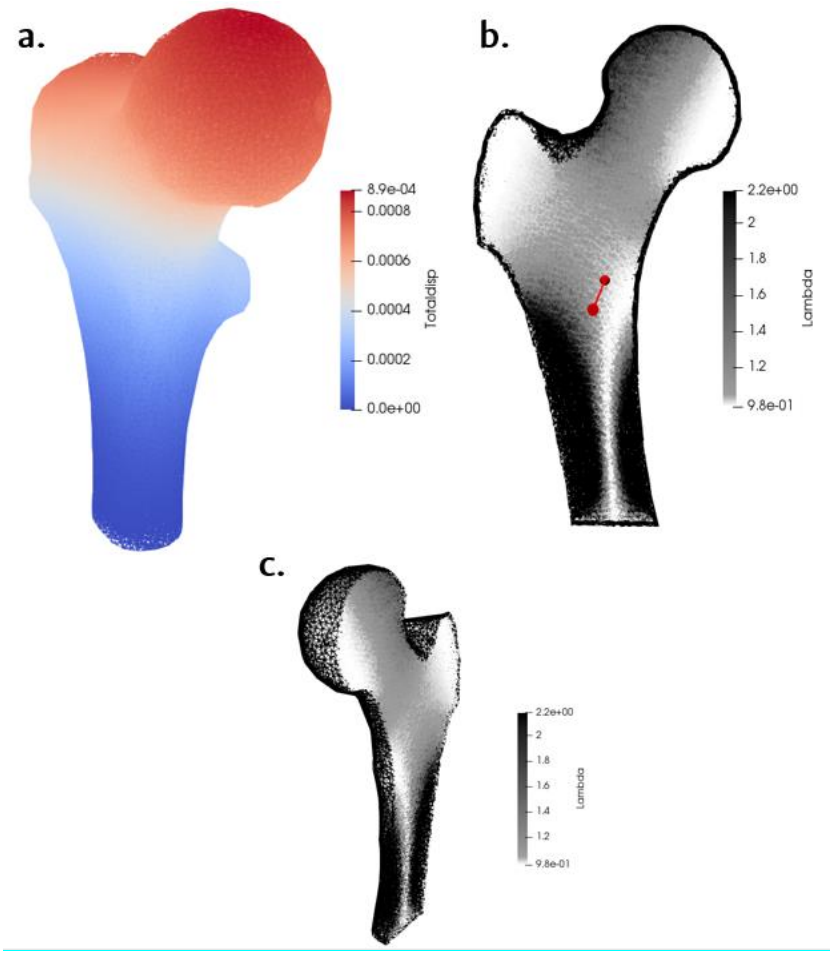

Fig. 18:(a) Total displacement for the loading history proposed by (Beaupre and Orr 1990). (b) Coronal section of the femur (c) Isometric view with a cut showing coronal section.

This last part in the paper is set as a starting point for future works in 3D and as proof that the methodology can be implemented in three dimensions with similar results as in 2D.

Discussion

In this work, a bone remodeling algorithm, based on the works of (Nackenhorst 1997; Garzón-Alvarado and Linero 2012) is proposed with a discrete element approach to address the bone remodeling problem, where an implementation is feasible in 2D and 3D. In addition, different aspects such as mesh quality, mesh size and mesh distribution were tested qualitatively to see the influence on the resultant topology.

In the first medical case, a zone with less density called Ward's triangle (in honor to Ward, who first described the internal structure of the proximal femur in 1938) can be seen between the ogival system of the trochanteric plateau and the cervicocephalic support system. This is an important region because cervicotrochanteric fractures originate here in people of advanced age (Martín and Kochen 2011). The calcar, which extends from the posteromedial cortex in the femoral neck to the distal part of the lesser trochanter, is identified with a high bone density in the final topologies. This is an

important fact since this region helps to support stems from implants, which need a dense cancellous bone for a proper anchorage; for this reason, numerous fixation methods have been proposed on this zone, see (Cha et al. 2019) and (Peng et al. 2020).

Among the obtained trabecular groups in the 2D simulations, it is noted that the greater trochanter group (GTM) appears as a less dense zone compared with the other groups. The secondary compressive (GSC) and secondary tensile (GST) groups are visible too: They begin to form in the lateral portion of the shaft and go upward forming an arch that ends in the vicinity of the greater trochanter. As seen in Fig. 14(c) the secondary groups meet at right angles, starting in the proximal section of the shaft, becoming gradually thinner as they approach the surface of the femoral head. These last observations agree well with our simulations as seen in Fig. 14(b). Another key feature found in the simulation is that a high bone density is predominant in zones where there is a greater cortical thickness as seen in Fig. 14(c) and Fig. 13; this helps to maintain the strength and rigidity of the femur as stated by (Marco et al. 2019). In the 3D simulations for the trabecular groups, the patterns corresponding to the principal trabecular groups have been achieved, although secondary groups as well as the greater trochanter groups do not show explicitly in the resultant topology, although there is bone density increase in those areas; these results differ from the 2D femur simulations, this might be due to the fact that (Beaupre and Orr 1990) results model better the two-dimensional domain.

The calcaneus bone is the largest tarsal bone and it is characterized by a cortex containing trabecular bone (Metcalf et al. 2018). Due to the mechanical stresses acting on the calcaneus, a set of trabecular groups are formed and play a crucial role in the biomechanics of this bone. These are important in orthopedic procedures and pathology treatments that compromise bone integrity such as in osteoarthritis therapy. The loading conditions were addressed as bone remodeling problems with the methodology proposed herein. The resulting trabecular groups resemble those seen in the calcaneus bone illustrated in Fig. 16(c). As in the previous medical case, a set of main trabecular groups have been identified as displayed in Fig. 16(b). These are in good agreement with anatomical studies regarding the biomechanics of calcaneus bone (Abboud 2018). The following trabecular motifs can be identified individually for the boundary conditions of (Belinha, Natal Jorge, and Dinis 2012): thalamic group (1); inferior plantar group (2); anterior apophyseal group (3); anterior plantar group (4); posterior achillean group (5); and central triangular area of refracted bone (6). An aspect that calls attention in some of these groups is the appearance of single lines corresponding to long trabecular groups such as the anterior apophyseal group or the central triangular area of refracted bone; this “thinning” could mean that the particular group does not play a vital structural role for that specific case load.

Having discussed the medical cases, it can be stated that this method may be used as an alternative to continuous domains due to its inexpensive computational cost as stated by (van Lenthe and Müller 2006) where even a 1000-fold reduction in processing time can be achieved by using frame elements, thus allowing to increase both the sample size and the complexity of the trabecular structure to analyze multiple loading configurations (Ruff1. Ruffoni, D. & Van Lenthe, G. H. 3.10 Finite element analysis in bone research: A computational method relating structure to mechanical function. Comprehensive Biomaterials II vol. 3 (Elsevier Ltd., 2017).oni and Van Lenthe 2017). A comparison in speed of the continuum and the proposed discrete methodology was briefly addressed as seen in Fig. 12(b) and Fig. 12(c): an improvement of more than 20% wall-clock time was achieved. Furthermore, it was found that the new bone remodeling approach using discrete structures have shown great potential.

A high level of mesh structuration leads to results quite similar to those obtained in TO. However, the simulations obtained with the medical cases which resemble the most to trabecular bone were those with non-structured meshes. This can be in part due to the fact that trabecular bone has been more accurately modeled with non-structured meshes (Luxner et al. 2009). This also agrees with the hypothesis given by (Weinans, Huiskes, and Grootenboer 1992) that trabecular bone is chaotically ordered and can be considered as a fractal since the best results were obtained with a triangular non-structured mesh.

Looking at the bone remodeling algorithm proposed, it is seen that the rule applied to each element is an objective function for an optimization process, relative to an external load. This function follows a preset value for the energy strain density. In this sense it can be said that this method uses a bio-inspired topology optimization.

Conclusions

The results show the self-enhancing process in which denser bone attracts more strain energy after each iteration, resulting in an even denser bone. This methodology when applied to the medical cases has proven to be a valid approach given the similarity with previous works (Garzón-Alvarado and Linero 2012; Valdez et al. 2017) and the anatomical features found in literature (Martín and Kochen 2011; Marco et al. 2019), and it has potential for 2D and 3D simulations .

As first stated by (van Lenthe and Müller 2006) the use of beam-like elements properly predicts the anatomical distribution of trabecular groups. A modelling approach using both beam elements for rod-like trabeculae and shell elements for plate-like structures, characteristic in cancellous bone, may be used to improve this methodology. However, the user must keep in mind that frame-based models alone fail to represent the plate-like networks, especially in certain areas where plate structures are

predominant in cancellous bone; so, this approach is applicable only to model mechanics of trabecular bone. In cortical bone, a precise model would need to be coupled with continuous elements to improve representation. This loss in precision to represent bone architecture is compensated with a gain in model simplification and solution time that could be used to look into nonlinear problems, typical in bone remodeling, or with several spatial scales. Another shortcoming of this approach, when dealing with medical cases, is that the initial domains are generated randomly in a manner that attempts to mimic cancellous bone, but not with a specific-patient domain. In further works, a more clinical accurate domain may be obtained from a specific portion of cancellous bone retrieved from a CT scan to evaluate bone remodeling in a specific loading case, this 3D simulation will benefit from the improvements in speed and simplicity from this methodology.

Finally, this work may be used by design engineers as a method to generate a concept design for biomaterial engineering applications since trabecular bone is a natural material that excels for its low weight and high mechanical performance (Ruff1. Ruffoni, D. & Van Lenthe, G. H. 3.10 Finite element analysis in bone research: A computational method relating structure to mechanical function. Comprehensive Biomaterials II vol. 3 (Elsevier Ltd., 2017).oni and Van Lenthe 2017). It could also be used too by medical researchers who are interested in the bone remodeling dynamics and the mechanical properties of cancellous bone with applications in bone grafts and implants. Furthermore, by understanding the topological optimization of bone remodeling, engineers should be inspired by these natural smart designs for developing sustainable and useful technologies.

References

Abboud, Fraser Harrold;Rami. 2018. “Biomechanics of the Foot and Ankle.” *Orthopaedic Knowledge Update: Foot and Ankle 5*, 3–12.

Annicchiarico, W., G. Martinez, and M. Cerrolaza. 2007. “Boundary Elements and β-Spline Surface Modeling for Medical Applications.” *Applied Mathematical Modelling* 31 (2): 194–208. https://doi.org/10.1016/j.apm.2005.08.021.

Beaupre, G S, and T E Orr. 1990. “An Approach for Time-Dependent Bone Modeling and Remodeling—Application: A Preliminary Remodeling Simulation - Beaupré - 2005 - Journal of Orthopaedic Research - Wiley Online Library.” *Journal of Orthopaedic …*, 662–70. http://onlinelibrary.wiley.com/doi/10.1002/jor.1100080507/abstract%5Cnpapers2://publication/uuid/9D5C378F-EDD8-4736-B052-510B4EFC85B9.

Belinha, J., R. M. Natal Jorge, and L. M.J.S. Dinis. 2012. “Bone Tissue Remodelling Analysis Considering a Radial Point Interpolator Meshless Method.” *Engineering Analysis with Boundary Elements* 36 (11): 1660–70. https://doi.org/10.1016/j.enganabound.2012.05.009.

Buenzli, P. R., P. Pivonka, and D. W. Smith. 2011. “Spatio-Temporal Structure of Cell Distribution in Cortical Bone Multicellular Units: A Mathematical Model.” *Bone* 48 (4): 918–26. https://doi.org/10.1016/j.bone.2010.12.009.

Cerrolaza, M., F. Nieto, and Y. González. 2018. “Computation of the Dynamic Compression Effects in Spine Discs Using Integral Methods.” *Journal of Mechanics in Medicine and Biology* 18 (5): 1–16. https://doi.org/10.1142/S0219519417501032.

Cesar, R., R. S. Boffa, L. T. Fachine, T. P. Leivas, A. M.H. Silva, C. A.M. Pereira, R. B.M. Reiff, and J. M.D.A. Rollo. 2013. “Evaluation of Trabecular Microarchitecture of Normal Osteoporotic and Osteopenic Human Vertebrae.” *Procedia Engineering* 59: 6–15. https://doi.org/10.1016/j.proeng.2013.05.087.

Cha, Yong Han, Jun Il Yoo, Seok Young Hwang, Kap Jung Kim, Ha Yong Kim, Won Sik Choy, and Sun Chul Hwang. 2019. “Biomechanical Evaluation of Internal Fixation of Pauwels Type III Femoral Neck Fractures: A Systematic Review of Various Fixation Methods.” *CiOS Clinics in Orthopedic Surgery* 11 (1): 1–14. https://doi.org/10.4055/cios.2019.11.1.1.

Cowin, S. C. 1986. “Wolff’s Law of Trabecular Architecture at Remodeling Equilibrium.” *Journal of Biomechanical Engineering* 108 (1): 83–88. https://doi.org/10.1115/1.3138584.

Daxner, Thomas. 2010. “Finite Element Modeling of Cellular Materials. In: Altenbach H., Öchsner A. (Eds) Cellular and Porous Materials in Structures and Processes. CISM International Centre for Mechanical Sciences, Vol 521. Springer, Vienna. Https://Doi.Org/10.1007/978-3-7091-0.” In , 634.

Ganghoffer, Jean François, and Ibrahim Goda. 2018. “Prediction of Size Effects in Bone Brittle and Plastic Collapse.” *Multiscale Biomechanics*, 345–88. https://doi.org/10.1016/B978-1-78548-208-3.50008-3.

Garzón-Alvarado, D. A., and D. Linero. 2012. “Comparative Analysis of Numerical Integration Schemes of Density Equation for a Computational Model of Bone Remodelling.” *Computer Methods in Biomechanics and Biomedical Engineering* 15 (11): 1189–96. https://doi.org/10.1080/10255842.2011.585972.

Geris, L., J. Vander Sloten, and H. Van Oosterwyck. 2010. “Connecting Biology and Mechanics in Fracture Healing: An Integrated Mathematical Modeling Framework for the Study of Nonunions.” *Biomechanics and Modeling in Mechanobiology* 9 (6): 713–24. https://doi.org/10.1007/s10237-010-0208-8.

González, Y., M. Cerrolaza, and C. González. 2009. “Poroelastic Analysis of Bone Tissue Differentiation by Using the Boundary Element Method.” *Engineering Analysis with Boundary Elements* 33 (5): 731–40. https://doi.org/10.1016/j.enganabound.2008.09.008.

Guevara, J. M., M. A. Moncayo, J. J. Vaca-González, M. L. Gutiérrez, L. A. Barrera, and D. A. Garzón-Alvarado. 2015. “Growth Plate Stress Distribution Implications during Bone Development: A Simple Framework Computational Approach.” *Computer Methods and Programs in Biomedicine* 118 (1): 59–68. https://doi.org/10.1016/j.cmpb.2014.10.007.

KOCH, JOHN C. 1993. “THE LAWS OF BONE ARCHITECTURE.” *From the Department of Anatomy, Johns Hopkins Medical School, Baltimore, Md.* 2 (6): 444–54.

Komarova, Svetlana V., Robert J. Smith, S. Jeffrey Dixon, Stephen M. Sims, and Lindi M. Wahl. 2003. “Mathematical Model Predicts a Critical Role for Osteoclast Autocrine Regulation in the Control of Bone Remodeling.” *Bone* 33 (2): 206–15. https://doi.org/10.1016/S8756-3282(03)00157-1.

Lemaire, Vincent, Frank L. Tobin, Larry D. Greller, Carolyn R. Cho, and Larry J. Suva. 2004. “Modeling the Interactions between Osteoblast and Osteoclast Activities in Bone Remodeling.” *Journal of Theoretical Biology* 229 (3): 293–309. https://doi.org/10.1016/j.jtbi.2004.03.023.

Lenthe, G. Harry van, and Ralph Müller. 2006. “Prediction of Failure Load Using Micro-Finite Element Analysis Models: Toward in Vivo Strength Assessment.” *Drug Discovery Today: Technologies* 3 (2): 221–29. https://doi.org/10.1016/j.ddtec.2006.06.001.

Luxner, Mathias H., Alexander Woesz, Juergen Stampfl, Peter Fratzl, and Heinz E. Pettermann. 2009. "A Finite Element Study on the Effects of Disorder in Cellular Structures." *Acta Biomaterialia* 5 (1): 381–90. https://doi.org/10.1016/j.actbio.2008.07.025.

Makris, Panagiotis A., Christopher G. Provatidis, and Demetrios A. Rellakis. 2006. "Discrete Variable Optimization of Frames Using a Strain Energy Criterion." *Structural and Multidisciplinary Optimization* 31 (5): 410–17. https://doi.org/10.1007/s00158-005-0588-z.

Marco, Miguel, Eugenio Giner, José Ramón Caeiro-Rey, M. Henar Miguélez, and Ricardo Larraínzar-Garijo. 2019. "Numerical Modelling of Hip Fracture Patterns in Human Femur." *Computer Methods and Programs in Biomedicine* 173: 67–75. https://doi.org/10.1016/j.cmpb.2019.03.010.

Martín, Raúl Álvarez San, and José Antonio Velutini Kochen. 2011. "Anatomía de La Cabeza Femoral Humana: Consideraciones En Ortopedia, Parte II. Biomecánica y Morfología Microscópica." *International Journal of Morphology* 29 (2): 371–76.

Martínez, G., and M. Cerrolaza. 2006. "A Bone Adaptation Integrated Approach Using BEM." *Engineering Analysis with Boundary Elements* 30 (2): 107–15. https://doi.org/10.1016/j.enganabound.2005.08.010.

Metcalf, Louis M., Enrico Dall'Ara, Margaret A. Paggiosi, John R. Rochester, Nicolas Vilayphiou, Graham J. Kemp, and Eugene V. McCloskey. 2018. "Validation of Calcaneus Trabecular Microstructure Measurements by HR-PQCT." *Bone* 106: 69–77. https://doi.org/10.1016/j.bone.2017.09.013.

Nackenhorst, Udo. 1997. "Numerical Simulation of Stress Stimulated Bone Remodeling." *Technische Mechanik* 17 (1): 31–40. http://www.uni-magdeburg.de/ifme/zeitschrift_tm/1997_Heft1/Nackenhorst.pdf.

Pawlikowski, Marek, Krzysztof Jankowski, and Konstanty Skalski. 2018. "New Microscale Constitutive Model of Human Trabecular Bone Based on Depth Sensing Indentation Technique." *Journal of the Mechanical Behavior of Biomedical Materials* 85 (May): 162–69. https://doi.org/10.1016/j.jmbbm.2018.05.036.

Peng, Matthew Jian Qiao, Hong Wen Xu, Hai Yan Chen, Ze Lin, Xin Xu Li, Chu Long Shen, Yong Qiang Lau, Er Xing He, and Yue Ming Guo. 2020. “Biomechanical Analysis for Five Fixation Techniques of Pauwels-III Fracture by Finite Element Modeling.” *Computer Methods and Programs in Biomedicine* 193: 105491. https://doi.org/10.1016/j.cmpb.2020.105491.

Pivonka, Peter, Jan Zimak, David W. Smith, Bruce S. Gardiner, Colin R. Dunstan, Natalie A. Sims, T. John Martin, and Gregory R. Mundy. 2008. “Model Structure and Control of Bone Remodeling: A Theoretical Study.” *Bone* 43 (2): 249–63. https://doi.org/10.1016/j.bone.2008.03.025.

Raggatt, Liza J., and Nicola C. Partridge. 2010. “Cellular and Molecular Mechanisms of Bone Remodeling.” *Journal of Biological Chemistry* 285 (33): 25103–8. https://doi.org/10.1074/jbc.R109.041087.

Ruff1. Ruffoni, D. & Van Lenthe, G. H. 3.10 Finite element analysis in bone research: A computational method relating structure to mechanical function. Comprehensive Biomaterials II vol. 3 (Elsevier Ltd., 2017).oni, D., and G. H. Van Lenthe. 2017. *3.10 Finite Element Analysis in Bone Research: A Computational Method Relating Structure to Mechanical Function*. *Comprehensive Biomaterials II*. Vol. 3. Elsevier Ltd. https://doi.org/10.1016/B978-0-12-803581-8.09798-8.

Sozen, Tumay, Lale Ozisik, and Nursel Calik Basaran. 2017. “An Overview and Management of Osteoporosis.” *European Journal of Rheumatology* 4 (1): 46–56. https://doi.org/10.5152/eurjrheum.2016.048.

Sun, Xiaoqiang, Yunqing Kang, Jiguang Bao, Yuanyuan Zhang, Yunzhi Yang, and Xiaobo Zhou. 2013. “Modeling Vascularized Bone Regeneration within a Porous Biodegradable CaP Scaffold Loaded with Growth Factors.” *Biomaterials* 34 (21): 4971–81. https://doi.org/10.1016/j.biomaterials.2013.03.015.

Valdez, S. Ivvan, Salvador Botello, Miguel A. Ochoa, José L. Marroquín, and Victor Cardoso. 2017. “Topology Optimization Benchmarks in 2D: Results for Minimum Compliance and Minimum Volume in Planar Stress Problems.” *Archives of Computational Methods in Engineering* 24 (4): 803–39. https://doi.org/10.1007/s11831-016-9190-3.

Vanegas-Acosta, J. C., N. S. Landinez P., D. A. Garzón-Alvarado, and M. C. Casale R. 2011. “A Finite

Element Method Approach for the Mechanobiological Modeling of the Osseointegration of a Dental Implant." *Computer Methods and Programs in Biomedicine* 101 (3): 297–314. https://doi.org/10.1016/j.cmpb.2010.11.007.

Walton, Dan, and Hadi Moztarzadeh. 2017. "Design and Development of an Additive Manufactured Component by Topology Optimisation." *Procedia CIRP* 60: 205–10. https://doi.org/10.1016/j.procir.2017.03.027.

Weinans, H., R. Huiskes, and H. J. Grootenboer. 1992. "The Behavior of Adaptive Bone-Remodeling Simulation Models." *Journal of Biomechanics* 25 (12): 1425–41. https://doi.org/10.1016/0021-9290(92)90056-7.

ANNEXES

Strain energy

$$W_{density} = 0.5 \cdot \underline{\sigma} \cdot \underline{\epsilon^T} = 0.5 \frac{\sigma_{xx}^2}{E}$$

$$U_{strain} = \iiint W_{density}\, dx\, dy\, dz = \int \int W_{density}\, dA dx = \frac{1}{2E} \int_A^{\cdot} \int_0^L \left(\left(\frac{P_i}{A} \right)^2 + \left(\frac{M_{(x)} z}{I} \right)^2 \right) dx\, dA$$

$$= \frac{1}{2E} \int_0^L \int_A^{\cdot} \left(\left(\frac{P_i}{A} \right)^2 + \left(\frac{M_{(x)} z}{I} \right)^2 \right) dA dx$$

$$\frac{1}{2E} \int_0^L \frac{P^2}{A} dx + \frac{1}{2E} \int_0^L \frac{M_x}{I^2} ds \int_A^{\cdot} z^2 dA$$

$$= \frac{1}{2} \int_0^L \frac{{P_i}^2}{EA} dx + \frac{1}{2} \int_0^L \frac{M^2(x)}{EI} dx$$

Solving the integral of the energy term due to the function moment M(x):

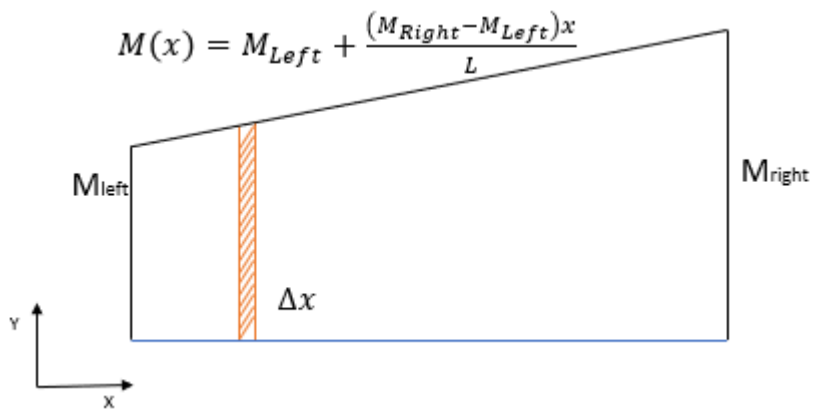

Fig. 19:Moment function along the element.

$$\int_0^L \left(M_L + \frac{M_R - M_L}{L}x\right)^2 dx = {M_L}^2 x + M_L\left(\frac{M_R - M_L}{L}\right)x^2 + \frac{1}{3}\left(\frac{M_R - M_L}{L}x\right)^2 x^3$$

$$= {M_L}^2 x + M_L\left(\frac{M_R - M_L}{L}\right)x^2 + \frac{1}{3}\left(\frac{M_R - M_L}{L}x\right)^2 x^3\Bigg]_{x=0}^{x=L}$$

$$= {M_L}^2 L + \frac{M_R M_L}{L}L^2 - \frac{{M_L}^2}{L}L^2 + \frac{1}{3}\left(\frac{{M_R}^2 - 2M_R M_L + {M_L}^2}{L^2}L^3\right)^2$$

$$= \frac{{M_L}^2 + {M_R}^2 + M_L \cdot M_R}{EI} \cdot L$$

So the total energy strain for each element is:

$$U_{strain} = \frac{1}{2}\sum_{i=1}^{N}\left[\frac{{P_i}^2 L_i}{E_i A} + \frac{1}{3}\cdot\frac{(M_i^{left})^2 + (M_i^{right})^2 + M_i^{left}.M_i^{right}}{E_i I}\cdot L_i\right]$$ (frame element) Eq. 6

$$U_{strain} = \frac{1}{2}\sum_{i=1}^{N}\left[\frac{{P_i}^2 L_i}{E_i A}\right]$$ (truss element)

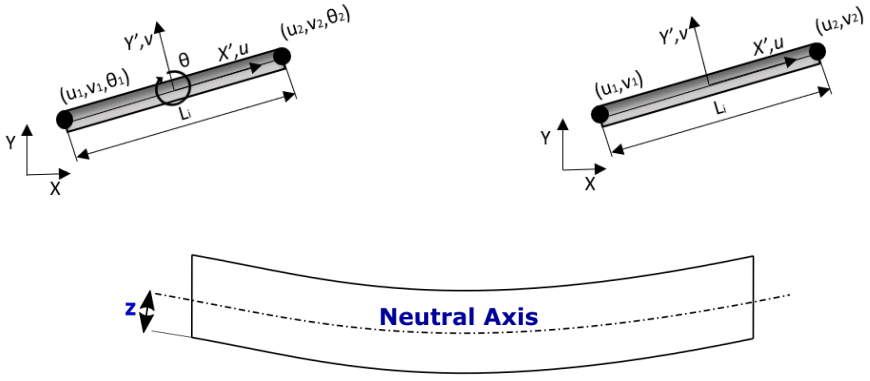

Fig. 20: Element formulation, frame (left) and truss (right).

Finite element, direct formulation Beam elements.

For a beam element the stiffness matrix is:

$$[K]_{Local} = \begin{bmatrix} \frac{12EI}{L^3} & \frac{6EI}{L^2} & \frac{-12EI}{L^3} & \frac{6EI}{L^2} \\ \frac{6EI}{L^2} & \frac{4EI}{L} & \frac{-6EI}{L^2} & \frac{2EI}{L} \\ \frac{-12EI}{L^3} & \frac{-6EI}{L^2} & \frac{12EI}{L^3} & \frac{-6EI}{L^2} \\ \frac{6EI}{L^2} & \frac{2EI}{L} & \frac{-6EI}{L^2} & \frac{4EI}{L} \end{bmatrix}$$

This local system can be seen in global form using the rotation matrix as follows:

$[K]_{global} = [T]^t [K]_{local} [T]$

where

$$[T] = \begin{pmatrix} \cos(\theta) & \sin(\theta) \\ -\sin(\theta) & \cos(\theta) \end{pmatrix}$$

The global system of equations is given by:

$$[F] = [K]_{global}[u] \quad \text{Eq. 3}$$

Finite element, direct formulation truss elements.

For a truss element the stiffness matrix is:

$$[K]_{Local} = \begin{pmatrix} \frac{EA}{L} & \frac{-EA}{L} \\ \frac{-EA}{L} & \frac{EA}{L} \end{pmatrix}$$

Finite element, direct formulation Frame elements.

The stiffness matrix can be obtained by superposition of the truss and beam elements, resulting in the following:

$$[K]_{Local} = \begin{bmatrix} \frac{AE}{L} & 0 & 0 & \frac{-AE}{L} & 0 & 0 \\ 0 & \frac{12EI}{L^3} & \frac{6EI}{L^2} & 0 & \frac{-12EI}{L^3} & \frac{6EI}{L^2} \\ 0 & \frac{6EI}{L^2} & \frac{4EI}{L} & 0 & \frac{-6EI}{L^2} & \frac{2EI}{L} \\ \frac{-AE}{L} & 0 & 0 & \frac{AE}{L} & 0 & 0 \\ 0 & \frac{-12EI}{L^3} & \frac{-6EI}{L^2} & 0 & \frac{12EI}{L^3} & \frac{-6EI}{L^2} \\ 0 & \frac{6EI}{L^2} & \frac{2EI}{L} & 0 & \frac{-6EI}{L^2} & \frac{4EI}{L} \end{bmatrix}$$

For a formulation using local coordinates as seen in Fig. 20, the following transformation can be used:

$[K]_{global} = [T]^t [K]_{local} [T]$

Where

$$[T] = \begin{bmatrix} \cos(\theta) & \sin(\theta) & 0 & 0 & 0 & 0 \\ -\sin(\theta) & \cos(\theta) & 0 & 0 & 0 & 0 \\ 0 & 0 & 1 & 0 & 0 & 0 \\ 0 & 0 & 0 & \cos(\theta) & \sin(\theta) & 0 \\ 0 & 0 & 0 & -\sin(\theta) & \cos(\theta) & 0 \\ 0 & 0 & 0 & 0 & 0 & 1 \end{bmatrix}$$

ABAQUS subroutine

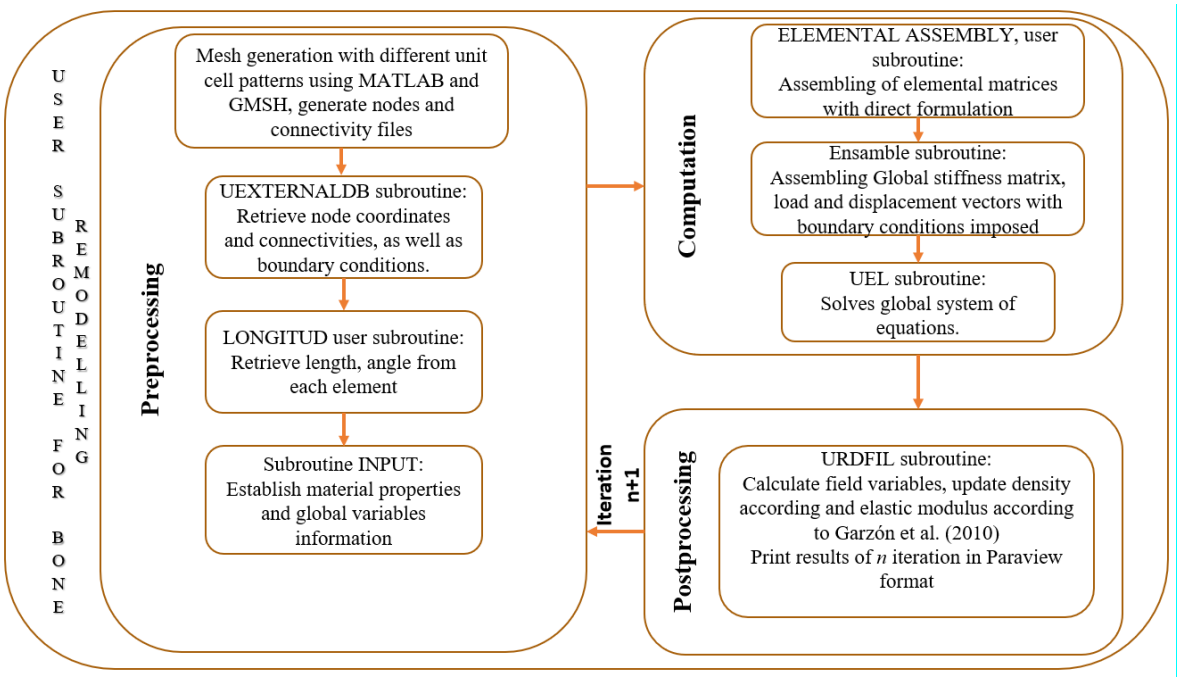

Fig. 21 :FE algorithm implemented in ABAQUS (2017).

Continuum Elements

An overview on how the finite element method (FEM) is used to solve the elasticity equations is shown in this section for the continuum elements, for triangular elements.

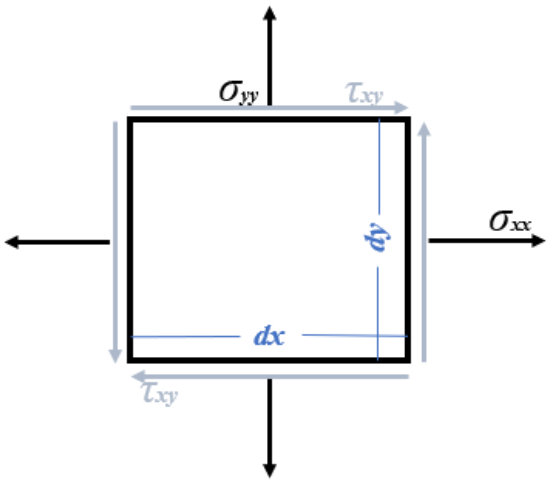

Fig. 22: Stress element.

Considering a differential stress element as seen in Fig. 22, the equilibrium equations are:

$$\sum F_x \rightarrow (\sigma_x)_{x+dx} t\, dy - (\sigma_x)_x t\, dy + (\tau_{xy})_{y+dy} t\, dx - (\tau_{xy})_y t\, dx + X t dx dy = 0$$

$$\sum F_y \rightarrow (\sigma_y)_{y+dy} t\, dx - (\sigma_y)_y t\, dx + (\tau_{xy})_{x+dx} t\, dy - (\tau_{xy})_x t\, dy + Y t dx dy = 0$$

Which yields the following differential equations:

$$\frac{\partial \sigma_x}{\partial x} + \frac{\partial \sigma_y}{\partial y} + X = 0$$

$$\frac{\partial \sigma_y}{\partial y} + \frac{\partial \tau_{xy}}{\partial y} + Y = 0$$

The information provided by the boundary conditions is included as the following equilibrium equations, according to Fig. 23:

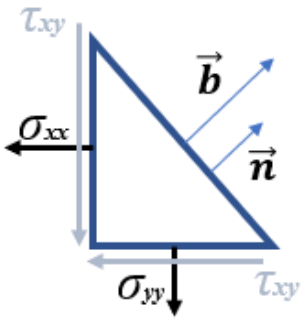

Fig. 23: Boundary element.

$$\sigma_x n_x + \tau_{xy} n_y - b_x = 0$$

$$\tau_{xy} n_x + \sigma_y n_y - b_y = 0$$

Plane strain

$$[D] = \frac{E}{(1-2\nu)(1+\nu)} \begin{bmatrix} 1-\nu & \nu & 0 \\ \nu & 1-\nu & 0 \\ 0 & 0 & \frac{1}{2}-\nu \end{bmatrix}$$

Plane stress

$$[D] = \frac{E}{(1-\nu^2)} \begin{bmatrix} 1 & \nu & 0 \\ \nu & 1 & 0 \\ 0 & 0 & \frac{1-\nu}{2} \end{bmatrix}$$

Postprocessing:

$$[\sigma] = [D]\,[\varepsilon]$$

$$[\sigma] = [D]\,L\,[U]$$

Where L is a differential operator:

Rearranging the following system of PDEs cab be obtained.

$$D_{11}\frac{\partial^2 u}{\partial x^2}+D_{12}\frac{\partial^2 v}{\partial x\partial y}+D_{33}\frac{\partial^2 u}{\partial y^2}+D_{33}\frac{\partial^2 v}{\partial x\partial y}+\bar{x}=0$$

$$D_{21}\frac{\partial^2 u}{\partial x\partial y}+D_{22}\frac{\partial^2 v}{\partial y^2}+D_{33}\frac{\partial^2 u}{\partial x\partial y}+D_{33}\frac{\partial^2 v}{\partial x^2}+\bar{y}=0$$

The finite element formulation will start using the Galerkin method to obtain a weak form of this system of equations. This process will be shown for equation for the first equation of the two.

$$\int_\Omega W\left(D_{11}\frac{\partial^2 u}{\partial x^2}+D_{33}\frac{\partial^2 u}{\partial y^2}\right)d\Omega+\int_\Omega W\left(D_{12}\frac{\partial^2 u}{\partial x\partial y}+D_{33}\frac{\partial^2 u}{\partial x\partial y}\right)d\Omega+\int_\Omega W\bar{x}d\Omega=0$$

The weak form can be obtained by applying integration by parts (divergence theorem) as follows:

$$\int_\Omega\left(D_{11}\frac{\partial W}{\partial x}\frac{\partial \hat{u}}{\partial x}+D_{33}\frac{\partial W}{\partial y}\frac{\partial \hat{u}}{\partial y}\right)d\Omega+\int_\Omega\left(D_{12}\frac{\partial W}{\partial x}\frac{\partial \hat{v}}{\partial y}+D_{33}\frac{\partial W}{\partial y}\frac{\partial \hat{v}}{\partial x}\right)d\Omega$$

$$-\int_\Gamma W\left(D_{11}\frac{\partial \hat{u}}{\partial x}n_x+D_{33}\frac{\partial \hat{u}}{\partial y}n_y\right)d\Gamma-\int_\Gamma W\left(D_{12}\frac{\partial \hat{v}}{\partial y}n_x+D_{33}\frac{\partial \hat{v}}{\partial x}n_y\right)d\Gamma-\int_\Omega W\bar{x}d\Omega=0$$

Is noted that the boundary conditions are added after applying integration by parts. Also, is useful to note that these terms can be expressed as:

$$\int_\Gamma W\left(D_{11}\frac{\partial \hat{u}}{\partial x}n_x+D_{33}\frac{\partial \hat{u}}{\partial y}n_y\right)d\Gamma+\int_\Gamma W\left(D_{12}\frac{\partial \hat{v}}{\partial y}n_x+D_{33}\frac{\partial \hat{v}}{\partial x}n_y\right)d\Gamma$$

$$=\int_\Gamma W(\sigma_x n_x+\tau_{xy}n_y)d\Gamma=\int_\Gamma W f_x d\Gamma$$

Using this expression, the weak formulation yields:

$$\int_\Omega\left(D_{11}\frac{\partial W}{\partial x}\frac{\partial \hat{u}}{\partial x}+D_{12}\frac{\partial W}{\partial x}\frac{\partial \hat{v}}{\partial y}\right)d\Omega+\int_\Omega\left(D_{33}\frac{\partial W}{\partial y}\frac{\partial \hat{v}}{\partial y}+D_{33}\frac{\partial W}{\partial y}\frac{\partial \hat{v}}{\partial x}\right)d\Omega=\int_\Omega W\bar{x}d\Omega+\int_\Gamma W f_x d\Gamma$$

Analogously the weak form of equation 11 is:

$$\int_\Omega\left(D_{33}\frac{\partial W}{\partial x}\frac{\partial \hat{u}}{\partial x}+D_{33}\frac{\partial W}{\partial x}\frac{\partial \hat{v}}{\partial y}\right)d\Omega+\int_\Omega\left(D_{21}\frac{\partial W}{\partial y}\frac{\partial \hat{v}}{\partial y}+D_{22}\frac{\partial W}{\partial y}\frac{\partial \hat{v}}{\partial x}\right)d\Omega=\int_\Omega W\bar{y}d\Omega+\int_\Gamma W f_y d\Gamma$$

By using Voight notation this can be expressed as:

$$\int_\Omega(L(W)^T[D]L[U])d\Omega=\int_\Omega W\bar{X}d\Omega+\int_\Gamma WFd\Gamma$$

Where:

$$[W] = \begin{bmatrix} W & 0 \\ 0 & W \end{bmatrix} \quad [U] = \begin{bmatrix} u \\ v \end{bmatrix} \quad [X] = \begin{bmatrix} x \\ y \end{bmatrix} \quad [F] = \begin{bmatrix} F_x \\ F_y \end{bmatrix}$$

$$\hat{u}^e(x) = \sum_{m=1}^{M} u_m N_m(x)$$

The next step is to discretize the domain so an approximation in an element will be:

$$t \int_{\Omega^e} (L(W)^T [D] L[U]) d\Omega^e = \int_{\Omega^e} W \bar{X} d\Omega^e + \mathrm{t} \int_{\Gamma^e} W F d\Gamma^e \qquad \text{Eq. 10}$$

In this form we can appreciate the problem in a simplified way as:

$$[K^e][U_m] = [F^e]$$

Where each term corresponds to those in Eq.10.

Given that the domain discretization gives place to irregular elements, a mapping of the domain is performed in each element that will facilitate numerical integration, in this case gaussian integration as seen Fig. 24.

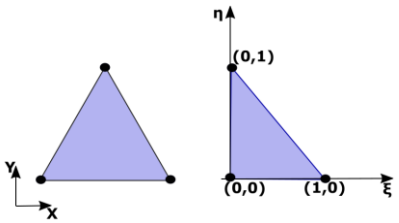

Fig. 24: Mapping to perform gaussian integration.

Using a local coordinate system (ξ,η) the elemental formulation yields:

$$L(\,) = \begin{bmatrix} \dfrac{\partial(\,)}{\partial x} & 0 \\ 0 & \dfrac{\partial(\,)}{\partial x} \\ \dfrac{\partial(\,)}{\partial x} & \dfrac{\partial()}{\partial x} \end{bmatrix} = \frac{1}{|J|} \begin{bmatrix} \dfrac{\partial y}{\partial \eta}\dfrac{\partial(\,)}{\partial \xi} - \dfrac{\partial y}{\partial \xi}\dfrac{\partial(\,)}{\partial \eta} & 0 \\ 0 & \dfrac{\partial x}{\partial \xi}\dfrac{\partial(\,)}{\partial \eta} - \dfrac{\partial y}{\partial \eta}\dfrac{\partial(\,)}{\partial \xi} \\ \dfrac{\partial x}{\partial \xi}\dfrac{\partial(\,)}{\partial \eta} - \dfrac{\partial y}{\partial \eta}\dfrac{\partial(\,)}{\partial \xi} & \dfrac{\partial y}{\partial \eta}\dfrac{\partial(\,)}{\partial \xi} - \dfrac{\partial y}{\partial \xi}\dfrac{\partial(\,)}{\partial \eta} \end{bmatrix} = \frac{1}{|J|} L^*(\,)$$

And the shape functions for a triangular linear node are:

$$N_i = \xi, N_j = \eta, \; N_k = 1 - \xi - \eta$$

These shape functions will be used approximate the displacement at each node, and the stiffness term $[K_{lm}]$ will be:

$$[K_{lm}] = \frac{t}{|J|}(L^*[W])^T[D](L^*[N_m])\int_\Omega d\xi \mathrm{d}\,\eta$$

The load vector can finally be expressed as the sum of both body and surface forces as:

$[F_l] = \int_{\Omega^e} W\bar{X}d\Omega^e + \mathrm{t}\int_{\Gamma^e} WFd\Gamma^e$

Density equation

The energy density is:

$$W(\rho) = \frac{1}{2\rho}\lambda^n\varepsilon^T C_0\varepsilon = \frac{\lambda^n}{\rho}\left[\frac{\varepsilon^T C_0\varepsilon}{2}\right] = \frac{\lambda^n}{\rho}U$$

The evolution density equation as stated by (Nackenhorst 1997) is:

$$\frac{d\rho}{dt} = k\left[\frac{W_\rho}{W_{ref}} - 1\right] \text{ Eq. 1}$$

Because $\lambda = \frac{\rho}{\rho_0}$ we can rearrange eq.X into:

$$\frac{d\lambda}{dt} = K\rho_0\left[\frac{\rho_0}{\rho_0}\frac{\lambda^n U}{\rho W_{ref}} - 1\right] = K\rho_0\left[\left[\frac{\rho_0}{\rho}\right]\frac{\lambda^n U}{\rho_0 W_{ref}} - 1\right] = K\rho_0\left[\lambda^{n-1}\frac{U}{\rho_0 W_{ref}} - 1\right]$$

And making:

$k_1 = K\rho_0$ and $\rho_0 W_{ref} = U_{ref}$

The dimensionless form of the evolution density equation can be written as:

$$\frac{d\lambda}{dt} = k_1\left[\lambda^{n-1}\frac{U}{U_{ref}} - 1\right] \text{Eq. 8}$$